Lieb-Robinson correlation function for long disordered transverse-field Ising chains

Brendan J. Mahoney
Department of Electrical Engineering, University of Notre Dame, Notre Dame, Indiana 46556, USA

Craig S. Lent*
Department of Electrical Engineering and Department of Physics and Astronomy, University of Notre Dame, Notre Dame, Indiana 46556, USA

(Received 27 December 2025; accepted 20 August 2026; published 8 September 2026)

The Lieb-Robinson correlation function can be used to characterize the propagation of quantum information in Ising chains. Considerable work has been done to establish *bounds* on this correlation function in various circumstances. To actually calculate the *value* of the correlation function directly typically requires a state space that grows exponentially with system size, and so is intractable for all but relatively small systems. We employ a recently developed method that enables direct calculation of the Lieb-Robinson correlation function and that scales linearly with system size. This enables the computation for systems with more than a thousand qubits, revealing the propagation of quantum information down the chain. We extend this technique to the problem of Ising chains with randomly disordered coupling strengths. Increasing disorder causes localization of the quantum correlations and halts propagation of quantum information down the chain. We see light-cone isocontours therefore becoming vertical. The decay of correlations down the chain is characterized by a correlation length that in the paramagnetic phase increases quadratically with mean coupling strength and inverse quadratically with disorder level. The correlation length peaks at the phase transition. We map our general expression for the correlation function in the Ising system onto the probability density in the single-particle tight-binding Su-Schrieffer-Heeger model for a specific initial condition.

DOI: 10.1103/xd68-dpwm

I. INTRODUCTION

The spread of information and correlations in quantum many-body systems is constrained in a fundamental way, even in the absence of relativistic causality. Lieb and Robinson showed that for a broad class of lattice Hamiltonians with local interactions, the growth of operator support is effectively limited by a finite velocity [1].

Their analysis considers local operators $\hat{A}_m$ and $\hat{B}_k$ acting on distinct subsystems k and m, with the time evolution of $\hat{A}_m$ given in the Heisenberg picture by

$$\hat{A}_m(t) = e^{i\hat{H}t/\hbar}\,\hat{A}_m(0)\,e^{-i\hat{H}t/\hbar}. \tag{1}$$

The growth of correlations between the two subsystems can be monitored through the norm of the commutator

$$C_{A,B}(t) = \|[\hat{A}_m(t), \hat{B}_k]\|. \tag{2}$$

If $k \neq m$, C is zero at $t = 0$ because the operators act on distinct subsystems, so the two operators commute. As time passes, $\hat{A}_m(t)$ spreads under Eq. (1) to include components with operators on subsystems other than m. When $\hat{A}_m(t)$ has significant components that act on subsystem k, the commutator can become nonzero, signaling the emergence of specifically quantum correlations between m and k.

Under general locality conditions, this quantity obeys the Lieb-Robinson (LR) bound

$$C_{A,B}(t) \leqslant K\,e^{-\mu(d_{k,m}-v_{\mathrm{LR}}t)}, \tag{3}$$

where $d_{k,m}$ is a measure of the distance between the subsystems, K and μ are system-dependent constants, and v_{LR} is the Lieb-Robinson velocity. Outside the effective light cone defined by this velocity, the commutator is exponentially small. This result has far-reaching implications, providing rigorous bounds on the locality of nonrelativistic quantum dynamics and establishing that correlations and entanglement can only propagate within a finite causal region set by the Lieb-Robinson velocity [2,3].

Considerable work has since refined and extended this framework. For short-range interacting Hamiltonians, tighter bounds have been obtained using a commutative graph construction [4], with subsequent improvements in related approaches [5,6]. Other directions have focused on systems with long-range couplings, where power-law interactions give rise to modified, nonlinear light cones [7–11]. These developments highlight the range of settings in which Lieb-Robinson techniques are now applied [12–14].

*Contact author: lent@nd.edu

Disorder represents a distinct and particularly rich direction. Anderson's work established that in one and two dimensions, arbitrarily weak disorder localizes all single-particle states, while in three dimensions a localization transition occurs at finite disorder [15,16]. This localization arises from quantum interference between closed-loop paths that enhances return probabilities and suppresses transport. In interacting spin systems, the impact of disorder was explored early on in studies of the transverse-field Ising model (TFIM) [17,18]. Building on Griffiths' original work on random ferromagnets [19], later analyses revealed how rare, strongly ordered regions can appear inside the disordered phase, producing unusual scaling behavior and strongly affecting the dynamics of the system [20–22].

When disorder is introduced, the standard linear light-cone structure implied by the Lieb-Robinson bound can be substantially modified. General analyses have revealed the emergence of logarithmic light cones in several disordered models, including the *XY* chain and related spin systems [23–29]. In many of these cases, the commutator obeys a bound of the form

$$C_{A,B}(t) \leqslant K|t|^{\alpha} e^{-\frac{d_{k,m}}{\xi}} = K e^{\alpha \ln(|t|)-\frac{d_{k,m}}{\xi}}, \tag{4}$$

where K and ξ are system-dependent constants that set the overall scale and spatial decay length of correlations, respectively. Here, the time dependence enters only as a power law rather than exponentially, resulting in an effective light cone that expands logarithmically in time. This behavior reflects the suppression of operator and information spreading created by disorder and provides a characterization of slow entanglement growth and constrained locality in disordered quantum phases. For the *XY* model with disorder, the Lieb-Robinson correlation function has been shown to be bounded under some conditions by a time-independent envelope [30,31].

It is usual either to study *bounds* on C or to calculate the actual values of C for relatively small systems. The reason for this is the familiar exponential explosion in the size of the state space for a multiqubit or spin system.

We focus here on the simplest dynamical system, a one-dimensional (1D) TFIM, with the aim of calculating the value of the LR correlation function for large systems and exploring the effects of disorder. To this end, we extend our recently developed method [32] for computing the LR correlation function on regular TFIM chains.

The simplicity of the TFIM model does not mean that it is without real-world applications [33]. It is a frequently applicable model for qubit arrays. Systems with thousands of qubits are now becoming available, making it possible to realize and study large many-body systems in controlled settings. Examples include entanglement generation in gate-defined quantum dots [34], coherent evolution in neutral-atom arrays [35], and quantum annealing experiments on large TFIM systems [36]. These developments make efficient theoretical methods for analyzing LR correlations in large systems increasingly important.

The present approach for studying the propagation of quantum correlations should be distinguished from state-based methods. A common technique is to solve the time-dependent Schrödinger equation for a state that is the ground state of an initial Hamiltonian H_0. At $t = 0$, the Hamiltonian is switched to a new Hamiltonian H, and the time evolution of the state is calculated, using various exact or approximate means. Such "quench" calculations have the great advantage of yielding all possible information in the quantum state over time. The disadvantages are that the results depend on the initial state and, as usual, are limited by the feasibility of representing the state space adequately. The LR correlation function is state independent, and so depends only on the system Hamiltonian. It is also a two-time correlation function—the correlation is between one qubit at $t = 0$ and another at some later time t. Finally, the time development of the LR correlation function is not a low-energy phenomenon; the full energy spectrum participates.

Section II briefly reviews the transverse-field Ising model and the operator Pauli walk (OPW) method for calculating the LR correlation function. The application of this method to the disordered chain is presented in Sec. III. Section IV discusses mapping our main results from the TFIM onto the Su-Schrieffer-Heeger (SSH) model. In Appendix A, we review Anderson localization in a single-particle 1D tight-binding chain, using techniques and visualizations we apply to the TFIM. This even simpler model provides a useful point of comparison. Appendix B provides an alternate formulation of the results of the operator Pauli walk method using Majorana operators.

II. OPERATOR PAULI WALK METHOD FOR THE ISING CHAIN

A. Transverse-field Ising model

We consider a 1D chain of N_q interacting qubits in states $|0\rangle$ or $|1\rangle$, or equivalently of spins $|\downarrow\rangle$ and $|\uparrow\rangle$ (we will use the description interchangeably). The system is described by the TFIM Hamiltonian with nearest-neighbor couplings:

$$H = -J \sum_{k=1}^{N_q-1} Z_k Z_{k+1} - \gamma \sum_{k=1}^{N_q} X_k. \tag{5}$$

Here, J denotes the coupling energy between qubits; we take $J \geqslant 0$. For a spin system, the X term can represent an applied transverse magnetic field. We interpret it here equivalently as representing the kinetic energy associated with the flipping dynamics of each qubit or spin. The presence of this term means that an isolated $|1\rangle$ (or $|\uparrow\rangle$) state is not a stationary state, but will precess in time. A natural timescale, related to the Rabi oscillation time for an isolated qubit, is in terms of the quantity

$$\tau = \frac{\pi\hbar}{\gamma}. \tag{6}$$

It is helpful then to measure time in terms of τ and energy in terms of γ. We define the dimensionless Hamiltonian

$$H' \equiv H/\gamma = -J' \sum_{k=1}^{N_q-1} Z_k Z_{k+1} - \sum_{k=1}^{N_q} X_k, \tag{7}$$

where $J' \equiv J/\gamma$.

The TFIM has two quantum phases separated by a critical point at $J' = 1$. Figure 1(a) shows the ground-state and first

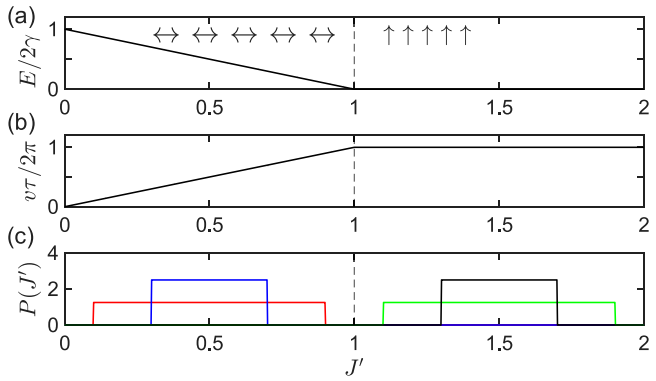

FIG. 1. Two phases of the TFIM chain. (a) Energies of the ground state and first excited state as a function of coupling J'. For $J' < 1$, the system is in the paramagnetic state; for $J' > 1$, it is in the ferromagnetic state. (b) Front velocity as a function of the coupling J' given by Eq. (9). (c) Probability distributions for disordered couplings as given by Eq. (19) with $J'_0 = 0.5$, $\Delta J' = 0.4$ (blue), and $\Delta J' = 0.8$ (red); and $J'_0 = 1.5$, $\Delta J' = 0.4$ (black), and $\Delta J' = 0.8$ (green).

excited-state energies for the system in the thermodynamic limit.

For $J' \leqslant 1$, we say the system is in the *paramagnetic* phase. When $J' = 0$, the chain consists of noninteracting spins whose energy eigenstates are each eigenstates of X_k: the symmetric ground state $|X^+\rangle = (|\uparrow\rangle + |\downarrow\rangle)/\sqrt{2}$ or antisymmetric excited state $|X^-\rangle = (|\uparrow\rangle - |\downarrow\rangle)/\sqrt{2}$. The ground state of the chain consists of all spins in the ground state. The first excited state of the system consists of a single site excited to the $|X^-\rangle$ state, which costs an energy 2γ. As the coupling J' is turned on, a single excitation on one site can move down the chain, delocalizing and lowering the energy. In this regime, we can think of the system quasiparticles as being roughly these mobile excitations.

For $J' > 1$, the system is in the *ferromagnetic* phase. For $J \gg \gamma$, the ground state of the whole chain consists of all sites in the $|\uparrow\rangle$ state or all in the $|\downarrow\rangle$ state. The Z_2 symmetry (flipping all the spins) produces a twofold degenerate ground state. For finite $J' > 1$, we can think of the quasiparticle excitations as domain walls in the chain: $|\cdots\uparrow\uparrow\uparrow\downarrow\downarrow\downarrow\cdots\rangle$. The motion of the domain wall is enabled by the nonzero kinetic energy term.

For both the paramagnetic and ferromagnetic phases with $0 < J' < \infty$, actual system eigenstates are delocalized combinations of these excitations, which mix the character of the simple quasiparticle descriptions above.

The TFIM can be mapped onto an equivalent fermion problem using the Jordan-Wigner transformation [37–39]. A subsequent Bogoliubov transformation rotates the fermion creation and annihilation operators to yield a free fermion Hamiltonian with bulk quasiparticle excitation spectrum:

$$E(q) = 2J\sqrt{g^2 + 1 - 2g\cos q}. \tag{8}$$

Here, q is the wave number of the harmonic excitation and $g \equiv 1/J'$. The energy eigenvalues for the system are all possible combinations of the quasiparticle excitation energies given by Eq. (8). The corresponding quasiparticle group velocities can

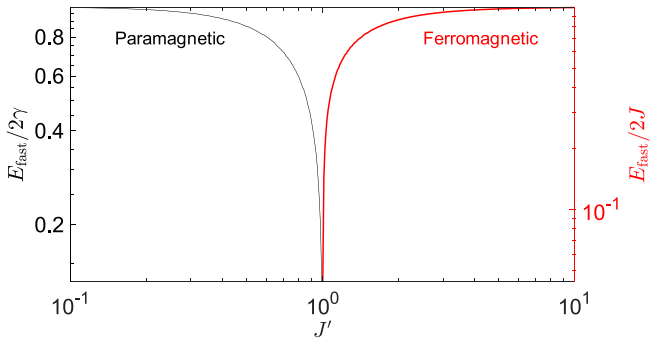

FIG. 2. The energy of the fastest quasiparticle.

be calculated via the usual expression $v(q) = (1/\hbar)\partial E/\partial q$. The maximum value over q of this velocity is given by

$$v\,\tau = \begin{cases} 2\pi J', & J' \leqslant 1, \\ 2\pi, & J' > 1. \end{cases} \tag{9}$$

A derivation is given in Ref. [32]. Figure 1(b) shows this velocity as a function of J'. As we will see below, this velocity represents the velocity of the correlation front that propagates down the chain; we therefore refer to it as the front velocity. In the context of quantum chaos, it is also known as the butterfly velocity.

We can define $E_{\rm fast}$ as the energy of the fastest quasiparticle, that is, the value of the energy in Eq. (8) for which the group velocity equals the maximum value given by Eq. (9). Figure 2 shows this quantity for both the paramagnetic and ferromagnetic phases. As suggested above, $E_{\rm fast}$ becomes 2γ in the extreme paramagnetic limit ($J' = 0$) and $2J'$ in the extreme ferromagnetic limit ($J' \gg 1$). At the critical point, this energy goes to 0.

There is another velocity that characterizes the propagation of the first-order effect of correlations, discussed in Refs. [32,40], but it reflects the initial turn-on of extremely small values of correlation and will not concern us here.

B. The operator Pauli walk method for the Lieb-Robinson correlation function

To characterize the dynamic spread of correlations, we study the Lieb-Robinson correlation function

$$C_k(t) \;=\; \|[Z_1(t), Z_k]\|, \tag{10}$$

which quantifies how correlations propagate as a function of time. We use the normalized Frobenius norm

$$\|\mathcal{O}\| = \sqrt{\frac{1}{2^{N_q}}\mathrm{Tr}(\mathcal{O}^\dagger\mathcal{O})}. \tag{11}$$

The operator $Z_1(t)$ evolves under $\hat{H}$ according to

$$Z_1(t) = \sum_{n=0}^{\infty} \frac{1}{n!}\pi^n i^n \left(\frac{t}{\tau}\right)^n [(\hat{H}')^n, Z_1]. \tag{12}$$

From the definition in Eq. (10), we see that at $t = 0$, Z_1 commutes with itself, and also with Z_k, which acts on a different site k, so $C_k(0) = 0$. The time evolution of Eq. (12) results in $Z_1(t)$ spreading to include components of Pauli operators on other sites. It follows from the Pauli operator commutation

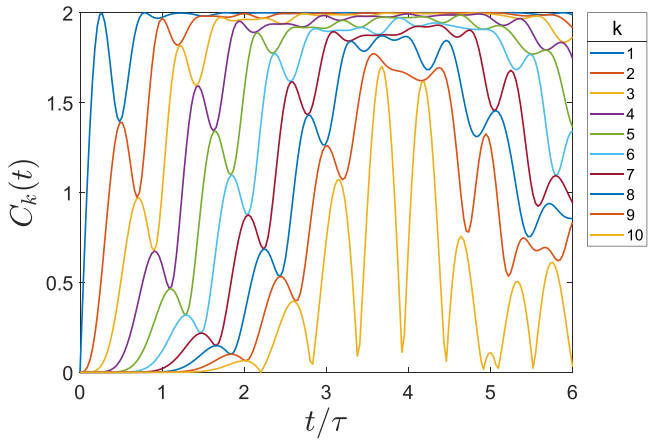

FIG. 3. The Lieb-Robinson correlation function for the TFIM of a ten-qubit chain with $J' = 1/2$. This is the result of a direct calculation using the definition of Eqs. (10) and (12).

relations (e.g., $[Z, X] = 2iY$) that the maximum value of $C_k(t)$ is 2.

For relatively short chains, it is tractable to calculate $C_k(t)$ directly from Eqs. (10) and (12). This requires calculating the matrix exponential of the $2^{N_q} \times 2^{N_q}$ Hamiltonian matrix. The result for a ten-qubit line is shown in Fig. 3. The correlation initially turns on for each site as the quantum influence propagates down the chain. The effect of reflections from the end of the chain, however, quickly becomes apparent, and indeed dominant. The computational challenge here is the same as that for direct state-based calculations, namely, that the size of the operators scales as 2^{N_q}, so for even modestly large systems direct calculations like this become untenable. For example, Colmenarez and Luitz [8] use heroic methods to calculate systems with $N_q = 22$.

Equations (10) and (12) provide the conceptual foundation for the OPW method introduced in Ref. [32], which addresses the problem of handling longer system sizes. A Pauli string is the tensor product of operators I_k, X_k, Y_k, or Z_k on each site; it is usual to suppress the identity operators notationally. Each nested commutation of $\hat{H}'$ with Z_1 generates a new Pauli string, corresponding to a "step" in an abstract operator space whose nodes represent Pauli strings and whose edges encode their coupling under $\hat{H}'$. The space of Pauli strings has dimension 4^{N_q}, and in general the whole space is required to support $Z_1(t)$ and therefore calculate $C_k(t)$. The OPW method exploits the fact that for the TFIM Hamiltonian H', the nested commutations in Eq. (12) explore only a much smaller structured subspace of size $2N_q$, forming a discrete walk that fully captures the dynamics.

To briefly illustrate, consider a four-qubit homogeneous chain. Starting from Z_1, evaluating any number of successive nested commutators with H'_{4q} in Eq. (12) generates only eight distinct Pauli strings:

$$Z_1,\ Y_1,\ X_1Z_2,\ X_1Y_2,\ X_1X_2Z_3,$$
$$X_1X_2Y_3,\ X_1X_2X_3Z_4,\ X_1X_2X_3Y_4. \tag{13}$$

These eight operators form the nodes of closed Pauli operator walks, shown schematically in Fig. 4. The weight of each directed edge represents the value of a commutator in

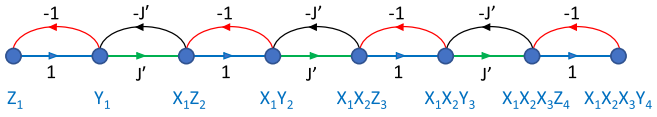

FIG. 4. Pauli operator walk for a four-qubit TFIM chain. The nodes correspond to the eight operator strings listed in Eq. (13), and the directed edges represent the value of commutators between Z_1 and terms in H'_{4q} that appear in Eq. (12).

the expansion given by Eq. (12). The sum in Eq. (12) maps onto a sum over all walks on the operator chain. Note that the walk is not along the qubit chain, but rather in this operator space. Thus, the nested commutators needed to calculate $Z_1(t)$ using Eq. (12) under the Ising Hamiltonian explore only a compact, linearly connected subset of the full, exponentially larger, space of Pauli strings.

The operator walks can be described using an adjacency matrix that takes the tridiagonal form

$$A_0 = \begin{pmatrix} 0 & 1 & 0 & 0 & 0 & 0 & \cdots & 0 \\ -1 & 0 & J' & 0 & 0 & 0 & \cdots & 0 \\ 0 & -J' & 0 & 1 & 0 & 0 & \cdots & 0 \\ 0 & 0 & -1 & 0 & J' & 0 & \cdots & 0 \\ 0 & 0 & 0 & -J' & 0 & \ddots & \vdots & \vdots \\ 0 & 0 & 0 & 0 & \ddots & \ddots & J' & 0 \\ \vdots & \vdots & \vdots & \vdots & \cdots & -J' & 0 & 1 \\ 0 & 0 & 0 & 0 & \cdots & 0 & -1 & 0 \end{pmatrix}. \tag{14}$$

As shown in Ref. [32], summing over all walks governed by this adjacency matrix yields the following closed-form expression for the LR correlation function on the homogeneous chain:

$$C_k^0(t) = \sqrt{\sum_{m=2k}^{2N_q} \left| 2\left[\exp\left(-2\pi \frac{t}{\tau} A_0\right)\right]_{1,m} \right|^2}. \tag{15}$$

Evaluating Eq. (15) requires calculating matrix exponentials of $\boldsymbol{A}_0$, a sparse real skew-symmetric matrix of size $2N_q \times 2N_q$. Using this approach, the LR correlation function can be calculated directly for any time without time marching or Trotterization. Because Eq. (14) scales only with $2N_q$, rather than 4^{N_q}, this approach allows $C_k(t)$ to be calculated for chains of hundreds or even thousands of qubits. As we shall see below, for many problems a finite chain can be long enough that the results essentially produce those of a semi-infinite chain.

Figure 5(a) shows snapshots of the LR correlation function $C_k(t)$ calculated using the OPW method at three different times. The Ising chain here is composed of $N_q = 1200$ qubits, though the correlation function is shown only for the first 600. In this case, $J' = 0.5$, so the system is in the paramagnetic phase. The front of quantum correlation moves smoothly down the line with the velocity given by Eq. (9) (i.e., $v = \pi$ qubits$/\tau$).

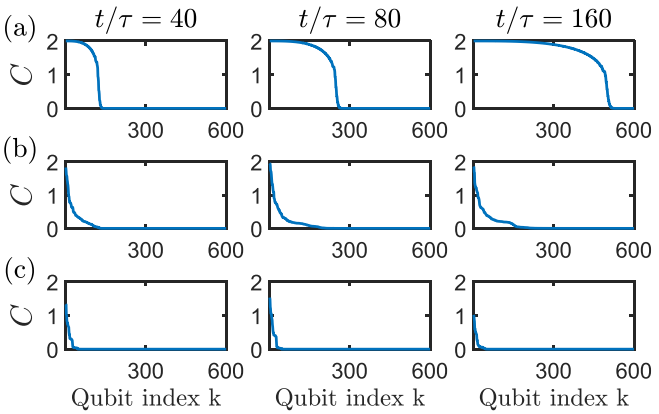

FIG. 5. Snapshots of the time evolution of $C_k(t)$ for a TFIM chain in the paramagnetic (weak-coupling) phase with $J_0' = 0.5$. (a) No disorder, $\Delta J' = 0$. (b) Weak disorder, $\Delta J' = 0.4$. (c) Strong disorder, $\Delta J' = 0.8$. The chain is 1200 qubits long, but only the first 600 qubits are plotted.

III. DISORDERED ISING CHAINS

We now generalize the homogeneous Ising chain to include spatially varying couplings. Working in the same dimensionless units, the inhomogeneous TFIM is

$$H' = -\sum_{k=1}^{N_q-1} J_k' Z_k Z_{k+1} - \sum_{k=1}^{N_q} X_k, \tag{16}$$

where J_k' is the coupling between sites k and $k+1$, which we again take to be non-negative but which can now vary down the chain. As in the homogeneous case, the nested-commutator dynamics of $Z_1(t)$ given by Eq. (10) is confined to a $2N_q$-dimensional operator subspace rather than the full 2^{N_q}-dimensional space of all Pauli strings. The only change is that the operator-space adjacency matrix acquires position-dependent weights:

$$A = \begin{pmatrix} 0 & 1 & 0 & 0 & 0 & 0 & \cdots & 0 \\ -1 & 0 & J_1' & 0 & 0 & 0 & \cdots & 0 \\ 0 & -J_1' & 0 & 1 & 0 & 0 & \cdots & 0 \\ 0 & 0 & -1 & 0 & J_2' & 0 & \cdots & 0 \\ 0 & 0 & 0 & -J_2' & 0 & \ddots & \vdots & \vdots \\ 0 & 0 & 0 & 0 & \ddots & \ddots & J_{N_q-1}' & 0 \\ \vdots & \vdots & \vdots & \vdots & \cdots & -J_{N_q-1}' & 0 & 1 \\ 0 & 0 & 0 & 0 & \cdots & 0 & -1 & 0 \end{pmatrix}. \tag{17}$$

Thus, the solution to the inhomogeneous problem requires only a straightforward substitution $\boldsymbol{A}_0 \to \boldsymbol{A}$. We sum over walks on the same set of operators; only the edge weights of the Pauli walk change. The LR correlation function therefore retains the same closed form, just in terms of the matrix $\boldsymbol{A}$:

$$C_k(t) = 2\sqrt{\sum_{m=2k}^{2N_q} \left| \left[\exp\left(-2\pi \frac{t}{\tau} A\right) \right]_{1,m} \right|^2}. \tag{18}$$

Within this inhomogeneous framework, we construct specific instances of disordered chains by independently sampling each coupling J_k' from a probability distribution. We use a uniform probability density centered at a baseline coupling J_0' with width $\Delta J'$:

$$P(J') = \begin{cases} \dfrac{1}{\Delta J'}, & \text{for } J' \in \left[J_0' - \frac{\Delta J'}{2},\, J_0' + \frac{\Delta J'}{2}\right], \\ 0, & \text{otherwise.} \end{cases} \tag{19}$$

Figure 1(c) illustrates the disorder distributions used in this paper. For the paramagnetic phase, we consider two cases centered at $J_0' = 0.5$: a weak-disorder distribution with $\Delta J' = 0.4$ (blue) and a strong-disorder distribution with $\Delta J' = 0.8$ (red). For the ferromagnetic phase, we use two analogous distributions centered at $J_0' = 1.5$, with $\Delta J' = 0.4$ (black) and $\Delta J' = 0.8$ (green).

For the case we consider here, with disorder in the couplings only, we define a simplified Ising parameter [20,41]

$$\delta \equiv [\ln(J')]_{\text{avg}}. \tag{20}$$

In the presence of disorder, the critical point is not at $J' = 1$, but rather at $\delta = 0$, usually corresponding to a value of J' slightly above 1. The parameter δ is negative for the paramagnetic phase and is positive for the ferromagnetic phase.

For the uniform distribution function in Eq. (19), we can calculate δ explicitly in terms of J_0' and $\Delta J'$, yielding

$$\delta = \frac{J_0'}{\Delta J'} \ln\left(\frac{J_0' + \Delta J'/2}{J_0' - \Delta J'/2}\right) + \frac{1}{2} \ln\left((J_0')^2 - \frac{(\Delta J')^2}{4}\right) - 1. \tag{21}$$

The parameter δ then varies strongly with J_0' for a fixed value of $\Delta J'$, but only weakly with $\Delta J'$ for fixed J_0'.

In the following sections, we calculate the disorder-averaged LR correlation function by considering N_c independently sampled configurations of the random couplings $\{J_k'\}^{(m)}$, where m is the index of a particular configuration of couplings. Then, the average value of the correlation function $\overline{C}$ is given by

$$\overline{C_k}(t) \equiv \frac{1}{N_c} \sum_{m=1}^{N_c} C_k^{(m)}(t), \tag{22}$$

where each $C_k^{(m)}(t)$ is evaluated from Eq. (18) for each particular sample. We similarly define the *typical* value C^{typ} as the geometric mean over the N_c sample configurations:

$$C^{\text{typ}}(k,t) \equiv \exp\left[\frac{1}{N_c} \sum_{m=1}^{N_c} \ln\left(C_k^{(m)}(t)\right)\right]. \tag{23}$$

Importantly, these two types of averages may yield quite different results in some circumstances [20].

A. Paramagnetic phase

We focus first on the results for the LR correlation function $C_k(t)$ in the paramagnetic (weak-coupling) phase, taking a baseline coupling of $J_0' = 0.5$.

Figure 5(b) shows snapshots of the LR correlation function $C_k(t)$ on a 1200-qubit chain (only the first 600 qubits are shown) for a specific random distribution of couplings drawn

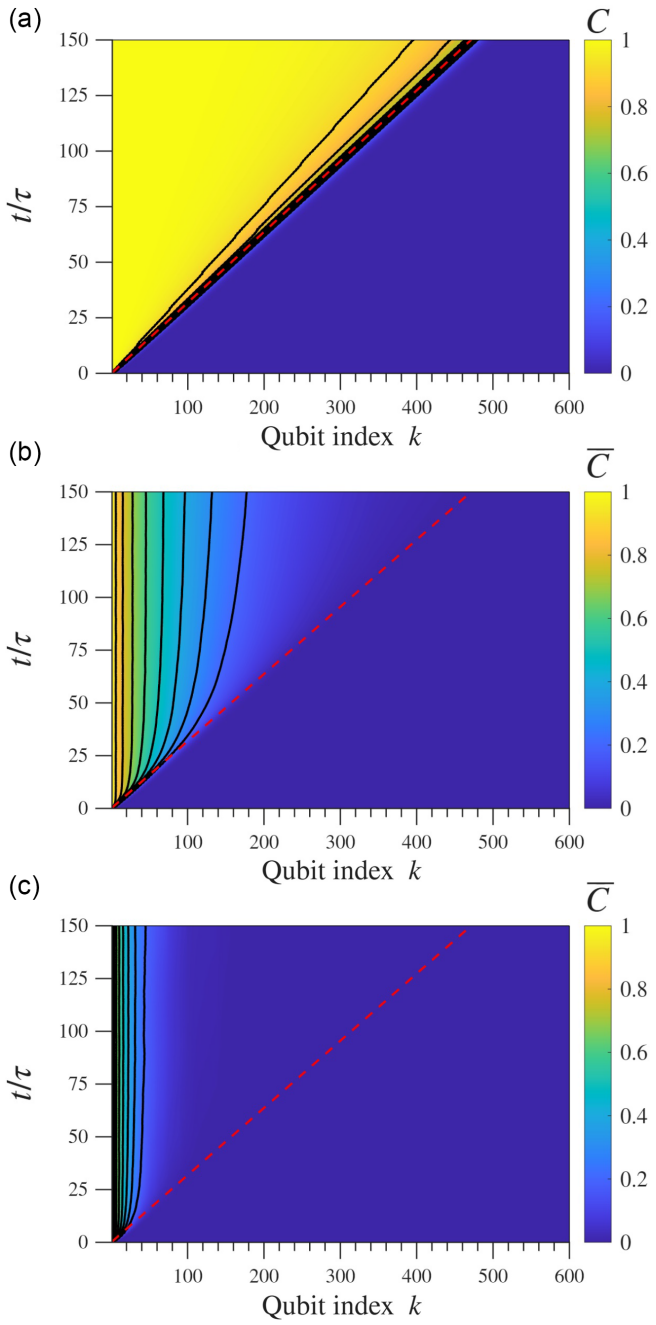

FIG. 6. Light-cone diagrams for Ising chain in the paramagnetic phase, $J' = 0.5$, with (a) no disorder, $\Delta J' = 0$, (b) weak disorder, $\Delta J' = 0.4$, and (c) strong disorder, $\Delta J' = 0.8$. In panels (b) and (c), the disorder-averaged mean value of the Lieb-Robinson correlation function $\overline{C}$ is plotted.

from Eq. (19) with $J'_0 = 0.5$ and $\Delta J' = 0.4$ ($\delta = -0.7212$). Figure 5(c) shows the case of $\Delta J' = 0.8$ ($\delta = -0.8307$). Increasing disorder in the coupling between qubits clearly impedes the propagation of quantum correlations down the chain.

Figure 6(a) shows the light-cone plot for the reference situation with no disorder, $\Delta J' = 0$, and $J'_0 = 0.5$. The color of the plot represents the value of $C_k(t)$ for this chain of 1200 qubits (600 are shown). Isocontours of C are shown for $C = [1, 0.9, 0.8, 0.7, 0.6, 0.5, 0.4]$. They are closely spaced together in this plot, but are indicated for comparison with the disordered cases below. The red dashed line corresponds to the propagation velocity given by Eq. (9). (Note that the slope of the line is the inverse of the velocity.) The light-cone plot is a fuller visualization of the snapshots of the moving correlation front in Fig. 5(a).

Figure 6(b) shows the light-cone plot for a 600-qubit disordered Ising chain with $J'_0 = 0.5$ and $\Delta J' = 0.4$ ($\delta = -0.7212$). Here, the color represents the configuration-averaged LR correlation function $\overline{C}$ defined in Eq. (22), averaged over $N_c = 500$ configurations. The probability density from which the values of J'_k are drawn is shown schematically in Fig. 1(c) in red. Isocontours are shown for the values of $\overline{C} = [1, 0.9, 0.8, 0.7, 0.6, 0.5, 0.4]$. The dashed red line in the light-cone plot again represents the velocity of the front in the disorder-free case. Close to the origin, the $\overline{C}$ isocontours follow the disorder-free velocity line, but they soon bend upward and the front velocity slows. As time progresses, the isocontours become closer and closer to vertical. This signifies that the front has stopped advancing: Correlations become stationary in space, marking the onset of localization.

The high-disorder light cone, with $\Delta J' = 0.8$ ($\delta = -0.8307$), is shown in Fig. 6(c). The probability density from which the values of J'_k are drawn is shown as the red curve in Fig. 1(c). The $\overline{C}$ isocontours in this case almost immediately turn vertical, corresponding to no propagation of the correlation front.

The light-cone diagrams in Figs. 6(b) and 6(c) display the mean correlation function $\overline{C}$. At the scale of the diagrams, similar plots of the geometric mean C^{typ} would be indistinguishable from those shown. That is true for the ferromagnetic regime discussed in the next section as well. We will examine the difference between the two means in Sec. III C.

The light-cone plots in Fig. 6 extend to time $t/\tau = 150$. If many-body localization has stopped the propagation of quantum correlations down the chain, we would expect to see the correlation function at longer times become stationary, i.e., independent of time. We can check this by examining $\overline{C}$ at two much longer times. Figure 7 shows the disorder-averaged LR correlation function for times t/τ=5000 (dots) and t/τ = 10 000 (solid lines). Here, we use a chain of N_q=1000 qubits and average over $N_c = 1000$ disorder configurations. The results are shown for various amounts of disorder: $\Delta J' = [0.2, 0.3, 0.4, 0.6, 0.8]$ corresponding to $\delta \in [-0.83, -0.69]$. The fact that the dots fall on the lines indicates that in each case the dynamics of the system has localized quantum correlations that are no longer moving down the chain—zero propagation velocity.

In both the light-cone plots of Fig. 6 and the later-time curves of Fig. 7, it is clear that higher amounts of disorder (larger $\Delta J'$) result in a more rapid decay of correlations down the chain. For example, in the $\Delta J' = 0.2$ case shown in Fig. 7, $\overline{C}$ is substantial out to several hundred qubits, whereas when $\Delta J' = 0.8$, it is extinguished a few tens of qubits down the chain. This observation can be made quantitative by calculating the qubit index for which $\overline{C}$ first drops below a threshold level for a late time, here chosen to be $t_{\text{late}}/\tau = 10\,000$. We define C_{thresh} as the threshold level (we use 0.2 below) and the

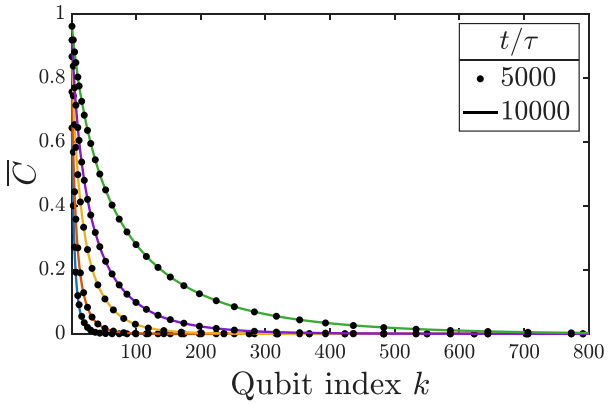

FIG. 7. Disorder-averaged LR correlation function in the paramagnetic phase for two late times. The TFIM chain is 1000 qubits in length with baseline coupling $J_0' = 0.5$. $\overline{C}(k,t)$ is averaged over 1000 disorder configurations. Results are shown at $t/\tau = 5000$ and $t/\tau = 10\,000$ for different disorder strengths: $\Delta J' = 0.2$ (green), $\Delta J' = 0.3$ (purple), $\Delta J' = 0.4$ (yellow), $\Delta J' = 0.6$ (red), and $\Delta J' = 0.8$ (blue). The identity of the two late-time curves (dots and lines) indicates that the penetration of quantum correlations down the chain in each case has become stationary.

corresponding qubit index λ,

$$\lambda(\Delta J') \equiv \min\{k : \overline{C}_k(t_{\text{late}}) \leqslant C_{\text{thresh}}\}. \tag{24}$$

The quantity λ then quantifies an effective localization length for the correlations. Figure 8 shows λ as a function of the disorder strength $\Delta J'$. The values are derived from the same 1000-qubit chain described in Fig. 7.

The inset in Fig. 8 shows a log-log plot of λ versus $\Delta J'$. The fitted slope of -2.07 is consistent with a $\lambda \sim 1/(\Delta J')^2$ dependence.

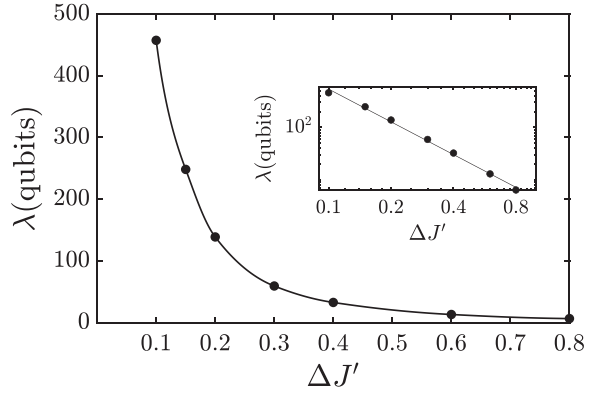

FIG. 8. Correlation length as a function of the coupling disorder. The system is 1000 qubits long with $J_0' = 0.5$, and the disorder is averaged over $N_c = 1000$ configurations. The analysis is for a late time, here $t/\tau = 10\,000$, by which point the LR correlation function has become stationary, as shown in Fig. 7. For each disorder strength $\Delta J'$, λ is the distance (in qubits) for which $\overline{C}_k$ drops below a threshold value, here 0.2. The decrease of λ with $\Delta J'$ quantifies the increasing spatial confinement of correlations as disorder grows.

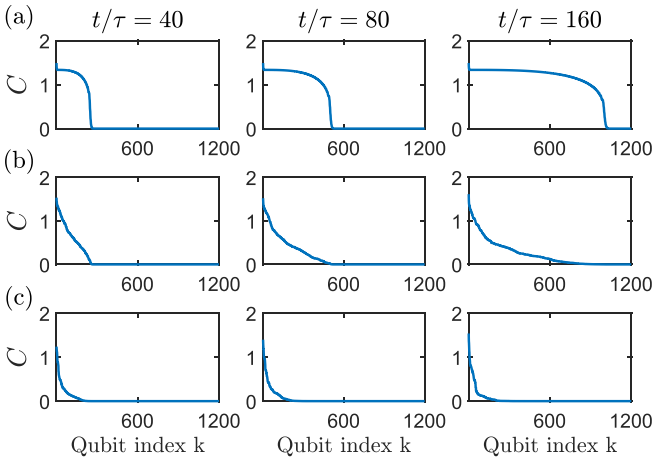

FIG. 9. Snapshots of the time evolution of $C_k(t)$ for a TFIM chain in the ferromagnetic (strong-coupling) phase with $J_0' = 1.5$. (a) No disorder, $\Delta J' = 0$. (b) Weak disorder, $\Delta J' = 0.4$. (c) Strong disorder, $\Delta J' = 0.8$.

B. Ferromagnetic phase

Figure 9(a) shows snapshots of the LR correlation function at three times for a 1200-qubit TFIM chain in the ferromagnetic phase, $J_0' = 1.5$, with no disorder, $\Delta J' = 0$. The quantum correlation front moves smoothly down the line with the velocity given by Eq. (9) (i.e., $v = 2\pi$ qubits$/\tau$), faster than that in the paramagnetic case shown in Fig. 5(a).

Figures 9(b) and 9(c) show snapshots of $C_k(t)$ for the same length chain and $J_0' = 1.5$, but with coupling disorder characterized by $\Delta J' = 0.4$ ($\delta = 0.4025$) and $\Delta J' = 0.8$ ($\delta = 0.3934$), respectively. These are each shown for one specific disorder configuration, drawn independently from the probability distribution of Eq. (19). We see that in the ferromagnetic phase, not only is the propagation faster than that in the paramagnetic phase, but also the quantum correlation penetrates down the chain farther. Higher disorder still impedes propagation and localizes the correlated region nearer the origin.

Figure 10(a) shows the light-cone plot of $C_k(t)$ for a disorder-free 600-qubit chain in the ferromagnetic phase with $J_0' = 1.5$. The color map represents the magnitude of the LR correlation function, and the overlaid isocontours are for levels $C = [1, 0.9, 0.8, 0.7, 0.6, 0.5, 0.4]$, though they are hard to separate visually. The red dashed line corresponds to the correlation front velocity of Eq. (9).

Figures 10(b) and 10(c) are light-cone plots of the disorder-averaged LR correlation function $\overline{C}_k(t)$ with $N_c = 500$. As above, $J_0' = 1.5$ and $\Delta J' = 0.4$ for the lower-disorder case, with $\Delta J' = 0.8$ for the higher-disorder case, corresponding to $\delta = 0.4025$ and 0.3934. Isocontours of $\overline{C}$ for the same levels as above are indicated. The red dashed line shows the front velocity for the disorder-free case. These light cones are qualitatively similar to those for the paramagnetic case shown in Fig. 6. In the absence of disorder, the correlation front moves ballistically down the chain, yielding straight light cones. Disorder in the couplings causes the light cones to bend upward and become vertical.

The group velocity is larger in the ferromagnetic phase than in the paramagnetic phase, as shown in Fig. 1(b). As

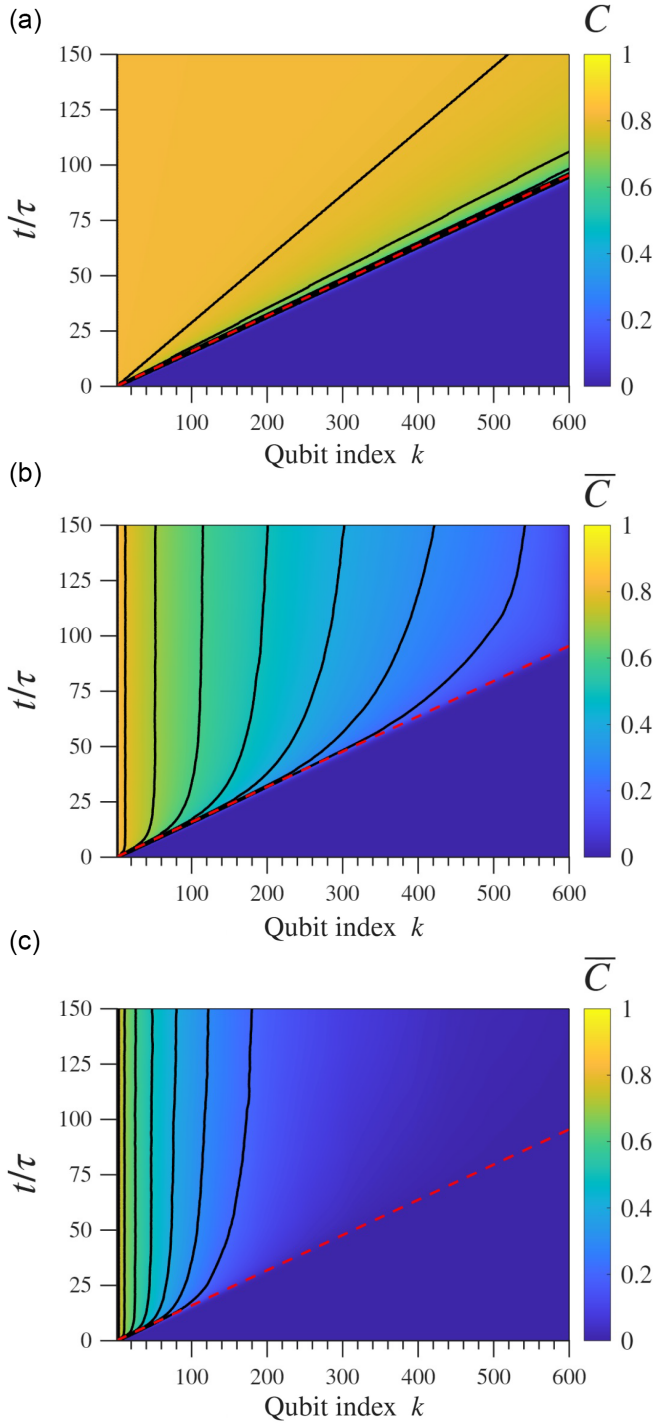

FIG. 10. Light-cone plots for Ising chain in the ferromagnetic phase, $J' = 1.5$ with (a) no disorder, $\Delta J' = 0$, (b) weak disorder, $\Delta J' = 0.4$, and (c) strong disorder, $\Delta J' = 0.8$. In panels (b) and (c), the disorder-averaged mean value of the Lieb-Robinson correlation function $\overline{C}$ is plotted.

a result, correlations are able to penetrate greater distances down the chain before being attenuated by scattering due to the disorder. The velocity does not further increase with J'_0, so the penetration down the chain does not continue to increase deeper into the ferromagnetic regime ($J'_0 \gg 1$).

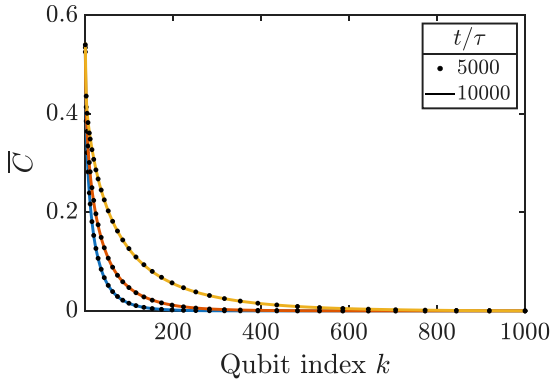

FIG. 11. Disorder-averaged LR correlation function in the ferromagnetic phase for two late times. The TFIM chain is 1000 qubits in length with baseline coupling $J'_0 = 1.5$. $\overline{C}(k,t)$ is averaged over 1000 disorder configurations. Results are shown at $t/\tau = 5000$ and $t/\tau = 10\,000$ for different disorder strengths: $\Delta J' = 0.4$ (yellow), $\Delta J' = 0.6$ (red), and $\Delta J' = 0.8$ (blue). The identity of the two late-time curves (dots and lines) indicates that the penetration of quantum correlations down the chain in each case has become stationary. Compared to the weak-coupling (paramagnetic) case shown in Fig. 7, correlations penetrate farther down the chain, corresponding to a larger localization length in the ferromagnetic phase.

As in the paramagnetic case, we can compare the LR correlation function at two late times to confirm that the propagation of quantum correlations has indeed ceased. Figure 11 shows the disorder-averaged correlation function $\overline{C}(k,t)$ at $t/\tau = 5000$ (dots) and $t/\tau = 10\,000$ (solid line) for a 1000-qubit system, averaged over $N_c = 1000$ disordered configurations, with $\Delta J' = [0.4, 0.6, 0.8]$, ($\delta \in [0.4025, 0.3934]$). The results indicate that the spatial profile has reached its stationary form. Again, it is clear that relative to the paramagnetic results of Fig. 7, the ferromagnetic correlations decay more slowly in k at each $\Delta J'$, indicating that correlations extend farther from the origin and the effective localization length is larger in the strong-coupling phase.

Hamza, Sims, and Stolz (HSS) found that under certain conditions, the LR correlation function for the disordered XY model (of which the Ising model is a special case) has a stationary exponential bound

$$C_k(t) \leqslant Ke^{-\alpha(k-1)}, \tag{25}$$

where α is a characteristic decay constant [30,31]. To compare this bound to our result, we evaluate the stationary disorder-averaged correlation profile $\overline{C}_k(t_{\text{late}})$ at time $t_{\text{late}}/\tau = 10\,000$. Figures 7 and 11 established that by this time the correlation front has ceased to propagate, so we can use $\overline{C}_k$ at t_{late} to represent the stationary correlation profile $\overline{C}(\infty)$.

We set $K = \overline{C}_1(t_{\text{late}})$ and then determine the largest decay constant α for which the inequality in Eq. (25) holds for all qubit indices k. That is, we find the α that optimally bounds our calculated result.

Figure 12 compares this exponential bound with our results for a 1000-qubit chain in the ferromagnetic phase with $J'_0 = 1.5$, $\Delta J' = 0.8$ ($\delta = 0.3934$), and $N_c = 1000$. These results conform to the HSS bound, but it is noticeable that the calculated correlations decay significantly faster. This holds

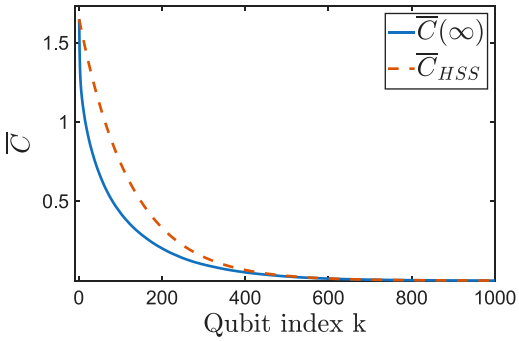

FIG. 12. Comparison between the disorder-averaged late-time LR correlation function and the exponential bound of Hamza, Sims, and Stolz [Eq. (25)]. The parameters for the calculation are $J_0' = 1.5$, $\Delta J' = 0.8$ ($\delta = 0.3934$), and $N_c = 1000$.

for both strong and weak disorder and for both paramagnetic and ferromagnetic phases.

C. Critical point region

In many respects, the behavior around the critical point $\delta = 0$ is very similar to that shown in Secs. III A and III B. The propagation behavior of Lieb-Robinson correlations largely varies smoothly as δ is varied across the quantum phase transition, so we do not produce them here. Light-cone diagrams shift smoothly from the behavior seen in the paramagnetic phase to that of the ferromagnetic phase. This is not unexpected since the correlation front moves at the speed given by Eq. (9) and illustrated in Fig. 1, a smoothly varying function.

Around the critical point, it is well known that Griffiths phases occur in the random TFIM [19,42,43]. These are rare regions with significant lengths of ferromagnetic order embedded in paramagnetic bulk regions, or vice versa. The occurrence of these phases can result in singularities in the scaling behavior of various equilibrium (or near-equilibrium) quantities such as the energy gap and the average ground-state expectation value of the surface magnetization [20]. One result is that the behavior of average quantities is sometimes quite distinct from typical quantities.

Can we see evidence of this divergence between the two means? Figure 13 compares the average Lieb-Robinson correlation function $\overline{C}_k$ with $C_k^{\rm typ}$ in the region around the critical point $\delta = 0$ ($J' \approx 1.015$) with $\Delta J' = 0.6$. The averages are over a set of $N_c = 20\,000$ samples, and the system has $N_q = 1200$ qubits. The time $t = 160\tau$ is chosen so that the system is essentially in its steady state, i.e., propagation of correlations down the chain has stopped.

The first observation to be made about the behavior shown in Fig. 13 is that over most of the region shown the arithmetic mean and geometric means are nearly indistinguishable from each other. However, a second observation is that down the chain, when the value of the correlation function is quite small, the two differ significantly. The inset shows the configuration-averaged correlations $\overline{C}$ and $C^{\rm typ}$ on a logarithmic scale in the region around $k = 1100$. By that point, the arithmetic mean is larger than the geometric mean by as much as 2 orders of magnitude. The reason for this is made apparent

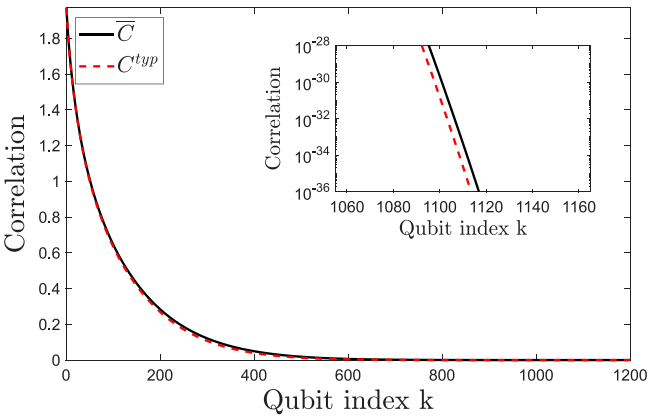

FIG. 13. The sample-averaged Lieb-Robinson correlation function for disorder that is centered on the critical point. Here, $N_q = 1200$, $J_0' = 1.0151$, $\Delta J' = 0.6$ ($\delta = 0$), $t = 160\tau$, and $N_c = 20\,000$. The arithmetic average $\overline{C}$ and the geometric average $C^{\rm typ}$ are nearly identical when the correlation is large, but are significantly different for very small values deeper in the chain.

in Fig. 14, which shows a histogram of the corresponding values of the correlation function C_k at three points along the chain: $k = 100, 400$, and 600. The range of the horizontal axis in each case is chosen so that all the values from the 20 000 samples are included. The red curves are fits to a log-normal probability distribution. As one moves down the chain, a few rare samples yield values of C that are much larger than those of the vast majority of other samples. As a result, the arithmetic mean is dominated by these rare cases.

It is perhaps tempting to attribute this to the presence of Griffiths phases, but there is reason for caution. Appendix A shows that a very similar phenomenon is evident in the much simpler system of a disordered tight-binding chain (see Figs. 20 and 21), a system without multiple phases. This suggests that the divergence between the two means may

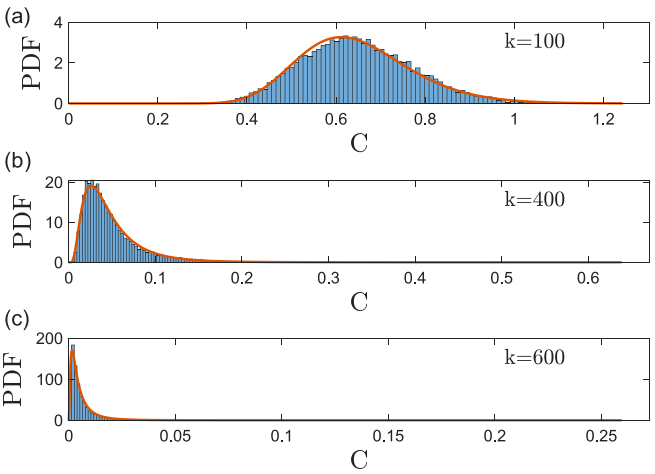

FIG. 14. Histograms of the distribution of values of C_k at different sites k down the chain. The parameters are the same as those for Fig. 13. The horizontal scales are chosen to include all values of C in the random samples. When C is small, there are some rare "lucky" samples with much larger values than most.

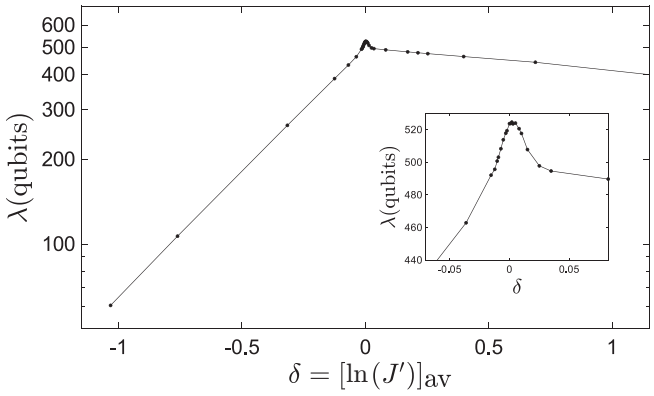

FIG. 15. The correlation length for the disordered TFIM for $\Delta J' = 0.6$ and various values of $J'_0 \in [0.4, 3.3]$ corresponding to the values shown for δ. The inset shows the peak on a linear vertical scale.

result simply from the multiplicative character of scattering from disorder in both the tight-binding and Ising chains. We also see a similar separation between geometric and arithmetic means of C for disordered Ising systems composed entirely of paramagnetic or ferromagnetic couplings.

Evidence for Griffiths phases is perhaps more apparent if we examine correlations in the region right around the quantum phase transition. Figure 15 shows the variation of the correlation decay length λ as the central coupling J'_0 (or equivalently δ) is varied. Here, $\Delta J' = 0.6$, the threshold value $C_{\text{thresh}} = 0.01$, and the number of samples N_c varies from 10 000 to 30 000 for each value of J'_0 (more samples are required to achieve convergence near the transition). The time $t = 160\tau$ is sufficiently long to show stationary behavior. In the paramagnetic domain to the left, $\lambda \sim (J'_0)^2$. In the ferromagnetic regime to the right, the correlation decay length varies quite slowly with J'_0. In a narrow region around $\delta = 0$, the decay length is enhanced. The inset shows the peak with a linear vertical scale for λ.

Using the language of quasiparticles [44–46], we also note that the peak in the correlation length at the critical point may be associated with the zero in the quasiparticle excitation energy at the phase boundary seen in Fig. 2. The disorder shifts the critical point from $J' = 1$ to $\delta = 0$ and changes a singularity to merely a peak.

IV. CONNECTION TO SU-SCHRIEFFER-HEEGER MODEL

Appendix A shows the qualitative similarity between the time evolution of the Lieb-Robinson correlation function $C_k(t)$ for the TFIM and the probability $P_R(k,t)$ [see Eq. (A6)] for a standard tight-binding chain. This similarity is quite general, including the decay due to random coupling disorder, and extends to the statistics of C_k and P_R. Because both quantities depend on the multiplicative effects of reflection and transmission at inhomogeneities, they both yield log-normal distributions.

We now show that in fact the expression for the Lieb-Robinson correlation function C_k in Eq. (18) can be rewritten in terms of the time evolution of the probability P_R for a very specific single-particle tight-binding-type Hamiltonian and a particular initial state. This makes the qualitative comparison in Appendix A quantitative and exact.

The SSH model [47,48] describes the motion of a single particle on a 1D chain of $2N$ sites under the Hamiltonian

$$H_{\text{SSH}} = v \sum_{k}^{N} |2k\rangle \langle 2k-1| + \text{H.c.} + \sum_{k}^{N-1} w_k |2k+1\rangle \langle 2k| + \text{H.c.} \tag{26}$$

Here, the $2N$ sites are coupled together in N unit cells, and v and w_n are the intracell and intercell hopping amplitudes, respectively. When all the w_n's are the same, this model exhibits two distinct phases depending on whether $|v| < |w|$ or $|v| > |w|$. We focus on the case when the intercell hopping terms w_n are not necessarily the same, introducing possible disorder. The matrix representation of H is given by

$$\boldsymbol{H}_{\text{SSH}} = \begin{pmatrix} 0 & v & 0 & 0 & 0 & 0 & \cdots & 0 \\ v & 0 & w_1 & 0 & 0 & 0 & \cdots & 0 \\ 0 & w_1 & 0 & v & 0 & 0 & \cdots & 0 \\ 0 & 0 & v & 0 & w_2 & 0 & \cdots & 0 \\ 0 & 0 & 0 & w_2 & 0 & v & \cdots & 0 \\ \vdots & \vdots & \vdots & \vdots & \ddots & \ddots & \ddots & \vdots \\ 0 & 0 & 0 & 0 & \cdots & w_{N-1} & 0 & v \\ 0 & 0 & 0 & 0 & \cdots & 0 & v & 0 \end{pmatrix}. \tag{27}$$

This bears a clear similarity to the matrix $\boldsymbol{A}$ in Eq. (17). We define

$$\boldsymbol{H}_A \equiv -iA. \tag{28}$$

The local gauge transformation

$$[\boldsymbol{U}]_{n,n'} = e^{i\pi n/2}\delta_{n,n'} \tag{29}$$

changes the sign of the lower-triagonal elements and transforms $\boldsymbol{H}_A$ into the dimensionless SSH Hamiltonian,

$$\boldsymbol{H}'_{\text{SSH}} = \boldsymbol{U}\boldsymbol{H}_A\boldsymbol{U}^{\dagger}, \tag{30}$$

if we make the identification $w_n/v \leftrightarrow J'_n$.

The time evolution of a state function on the SSH chain is given by

$$\psi_{\text{SSH}}(t) = e^{-i2\pi H'_{\text{SSH}}(t/\tau)}\psi_{\text{SSH}}(0). \tag{31}$$

We can therefore directly connect the time evolution of the TFIM Lieb-Robinson correlation function $C_k(t)$ with the time evolution of the wavefunction on an SSH chain using the techniques shown in the Appendix for a standard tight-binding chain. We choose an initial state at the first SSH site

$$\langle k|\psi_{\text{SSH}}(0)\rangle = \delta_{k,1} \tag{32}$$

and calculate

$$P^{\text{SSH}}(n,t) = |\langle n|e^{-i2\pi H'_{\text{SSH}}(t/\tau)}\psi_{\text{SSH}}(0)\rangle|^2, \tag{33}$$

the probability of finding the particle on site n at time t, given that it was on site 1 at time $t = 0$. If we define $P_R^{\text{SSH}}(k,t)$ for $k \in [1,N]$ to be the probability of finding the particle at time

t to the right of SSH site $2k-1$,

$$P_R^{\rm SSH}(k,t) = \sum_{m=2k}^{2N_q} P^{\rm SSH}(m,t), \tag{34}$$

the expression in Eq. (18) can be written as

$$C(k,t) = 2\sqrt{P_R^{\rm SSH}(k,t)}. \tag{35}$$

Equation (35) links the spread of probability in an SSH chain to the spread of the Lieb-Robinson correlation function in a TFIM chain. Mathematically and in terms of computational ease, Eq. (35) is precisely equivalent to Eq. (18). The basis states for $H'_{\rm SSH}$ map onto the operators determined by the OPW method as illustrated in Fig. 4, which it should be noted are the Majorana operators for the spin chain. The state-independent quantity $C_k(t)$ for the many-body TFIM for N_q spins is connected by Eq. (35) exactly to the evolution of the single-particle state defined on the $2N_q$ SSH sites with the initial state given by Eq. (32).

V. DISCUSSION

Seeing the precise form that the Lieb-Robinson correlation function takes as quantum correlations move down a long Ising chain can be very revealing. This calculation is crucially enabled by the operator Pauli walk method [32]. Figures 11 and 12 show calculations on a 1000-qubit chain. To represent either a quantum state or quantum operators on the chain would require a basis of size $2^{1000} \approx 10^{301}$, a number that greatly exceeds the number of particles in the visible universe. In contrast, evaluating Eq. (18) for $C_k(t)$ requires a basis size of only 2000. This is all the more important for assessing directly the effects of disorder because of the need to average over many random configurations. Of course, the quantum state contains vastly more information than the correlation function.

As we have seen, another feature of the OPW result in Eq. (18) beyond treating arrays that are very long is that it can be used to compute the LR correlation function at any time, including very long times, without time marching or Trotterization. This makes it possible to see directly that the light cones for the disordered Ising chain are not logarithmic, but in fact become vertical (zero velocity), in agreement with the bound of Hamza, Sims, and Stolz [30,31].

The analysis of the single-particle tight-binding chain in Appendix A illustrates the key features of disorder-induced localization using the same approach we subsequently employed in Sec. III. The examination of the statistics of $P_R(x)$ also shows that one feature observed in the Ising results—the difference between the arithmetic and geometric means—is actually a generic feature of the multiplicative nature of multiple-scattering systems [46].

The method we have employed is not general purpose. The closed nature of the walk in the OPW method is a consequence of the fact that the Ising Hamiltonian can be written as a quadratic in the Majorana operators that form the operator basis set [e.g., those in Eq. (13)]. For example, including next-near-neighbor interactions would yield an explosion in the number of operators required. The method is also limited to correlations between the first qubit in the chain and the kth qubit.

In Ref. [49], Roösz, Lin, and Iglói use a Majorana basis for calculating the relaxation of the average magnetization from a quench for the disordered TFIM. We show in Appendix B that using such a basis provides an alternate derivation for the results from our operator Pauli walk method.

The mapping of the Ising Lieb-Robinson correlation function, which is importantly state independent, onto the evolution of a *particular* state for the SSH model provides another interpretation of the main result [Eq. (18)] and may suggest further avenues for exploration. The linkage between the two models is well known, as is the occurrence of zero-energy edge modes in both.

It would be a mistake to conclude that the many-body localization seen in the TFIM is just the Anderson localization of a quasiparticle. The full excitation spectrum of the TFIM Hamiltonian includes the presence of all possible quasiparticles. We have not limited the analysis to the transport of a single quasiparticle; all are included in the correlation function. Similarly, there is no restriction to only low-energy excitations. The localization in this many-body system must be localization of all quasiparticle excitations.

The primary result of this work is the calculation of the Lieb-Robinson correlation function, rather than a bound on it, in the case of disorder. Quantum correlations and information are localized and not able to propagate farther down the chain. Extending the techniques that made this possible is a subject for further study.

DATA AVAILABILITY

There are no publicly available research data or software supporting this manuscript. Requests for further information or data should be sent to the authors.

APPENDIX A: THE TIGHT-BINDING CHAIN: DISORDER AND ANDERSON LOCALIZATION

1. Basic model

We first consider a single particle moving on a 1D chain with no disorder. The Hamiltonian for a tight-binding chain of N sites can be written as

$$\hat{H} = -\gamma \sum_{k=1}^{N-1} [|k+1\rangle\langle k| + |k\rangle\langle k+1|], \tag{A1}$$

where the hopping matrix element is γ, which we take to be positive. The on-site potentials are taken to be zero because they play no role here; this simply sets the zero of energy. The characteristic time is given by

$$\tau \equiv \frac{\pi\hbar}{\gamma}. \tag{A2}$$

In the thermodynamic limit, the energy eigenstates can be labeled by a wave number q and the eigenenergies are given by

$$E(q) = -2\gamma\cos(q). \tag{A3}$$

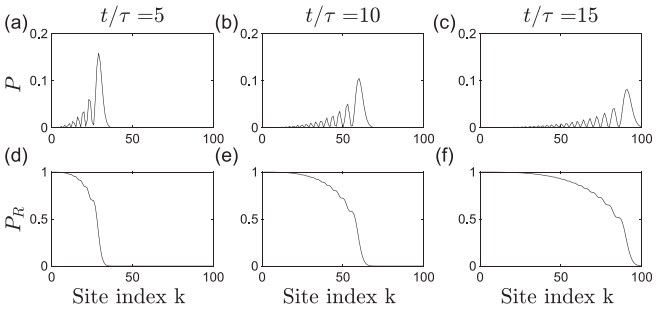

FIG. 16. Snapshots of the probability for a tight-binding chain of 600 sites. $P(k,t)$, the probability of finding the particle at site k, is shown at different times in panels (a)–(c). The probability $P_R(k,t)$ of finding the particle to the right of site k is shown in panels (d)–(f).

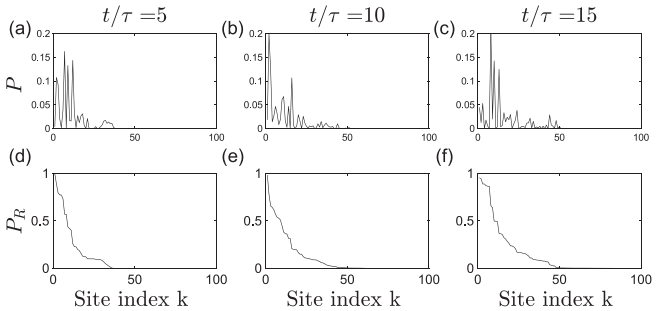

FIG. 17. Snapshots of the probability for the tight-binding chain of 600 sites with disorder. The site probability $P(k,t)$ is shown in panels (a)–(c). The probability of finding the particle to the right of site k, $P_R(k,t)$ is shown in panels (d)–(f). The disorder in the hopping matrix element is characterized by $\Delta\gamma/\gamma_0 = 1$.

We define the velocity v as the maximum group velocity; thus,

$$v\,\tau = \tau \frac{1}{\hbar}\frac{\partial E}{\partial q}\bigg|_{\max} = 2\pi. \tag{A4}$$

2. Disorder-free case

We are interested in the case in which the particle is initially localized on the first site, so $\Psi(k,0) = \delta_{k,1}$. We solve for the time-dependent wavefunction by directly performing the unitary transformation

$$\Psi(k,t) = e^{-i\hat{H}t/\hbar}\,\Psi(k,0). \tag{A5}$$

The probability density at site k and time t is then $P(k,t) = |\Psi(k,t)|^2$.

Figures 16(a)–16(c) show snapshots of the probability density for a line of $N = 600$ sites at times $t/\tau = [5, 10, 15]$. The probability peak moves down the chain with the velocity given by Eq. (A4) (i.e., $v = 2\pi$ sites$/\tau$).

To connect the evolution of the probability $P(k,t)$ with the Lieb-Robinson correlation function in the TFIM, we first define

$$P_R(k,t) = \sum_{k'=k+1}^{N} P(k',t), \tag{A6}$$

the probability of finding the particle somewhere to the right of site k at time t. Figures 16(d)–16(f) show snapshots of P_R for the same times as above. The front moves down the chain with velocity v. The sites ahead of the front do not yet "know" about the particle that was at site 1 at time $t = 0$. The light-cone plot of $P_R(k,t)$ for this system is shown in Fig. 18(a). The dashed red line corresponds to the front motion. It has a slope of $1/(2\pi)$ corresponding to the velocity in Eq. (A4); because the time is shown on the vertical axis, the front velocity is the inverse of the line's slope.

3. Disordered case—Anderson localization

We now consider the case where the hopping matrix elements between sites vary randomly down the chain. We are not considering the case with varying on-site potentials simply because variable hopping is most clearly analogous to the TFIM with disordered couplings between spins, which is our primary focus. The Hamiltonian is then

$$\hat{H} = -\sum_{k=1}^{N-1} \gamma_k [|k+1\rangle\langle k| + |k\rangle\langle k+1|]. \tag{A7}$$

The matrix elements γ_k are independently drawn from a uniform probability distribution centered at γ_0 with width $\Delta\gamma$:

$$P(\gamma) = \begin{cases} \dfrac{1}{\Delta\gamma}, & \text{for } \gamma \in \left[\gamma_0 - \frac{\Delta\gamma}{2},\ \gamma_0 + \frac{\Delta\gamma}{2}\right], \\ 0, & \text{otherwise.} \end{cases} \tag{A8}$$

A particular set of $N-1$ randomly chosen γ_k's constitutes a specific disorder configuration for the tight-binding chain. We solve for the unitary time evolution of the state function under Eq. (A7) and compute the probabilities P and P_R as before. Figure 17 shows snapshots of the time evolution of both probabilities for a specific disorder configuration chosen from a distribution with $\Delta\gamma/\gamma_0 = 1$. The snapshots are at times $t/\tau = [5, 10, 15]$, where $\tau \equiv \pi\hbar/\gamma_0$. It is clear even in this single sample that, when compared with the nondisordered case of Fig. 18(a), the particle propagation is impeded by the multiple reflections caused by the disorder.

Of more interest than the behavior of a specific disorder configuration is the average behavior. We define $\overline{P}_R$ as the configuration average of P_R,

$$\overline{P}_R(k,t) = \frac{1}{N_c}\sum_{m_c}^{N_c} P_R^{(m_c)}(k,t), \tag{A9}$$

where m_c is the index of a specific disorder configuration and N_c is the total number of such configurations sampled.

Light-cone plots of $\overline{P}_R$ for the cases of $\Delta\gamma/\gamma_0 = 1$ (weak disorder) and $\Delta\gamma/\gamma_0 = 2$ (strong disorder) are shown in Figs. 18(b) and 18(c), respectively. Here, $N = 300$ sites, though the plots only extend over half that length. The number of disorder configurations in the average is $N_c = 20\,000$. Contours of constant $\overline{P}_R = [0.01, 0.02, 0.05, 0.1, 0.2, 0.3, 0.4, 0.5, 0.6, 0.7, 0.8]$ are indicated by black lines. The red dashed line in each figure corresponds to ballistic propagation with velocity $v = 2\pi/\tau$ as seen in Fig. 18(a).

The light-cone plots of Figs. 18(b) and 18(c) reveal that the disorder suppresses particle motion. This is the

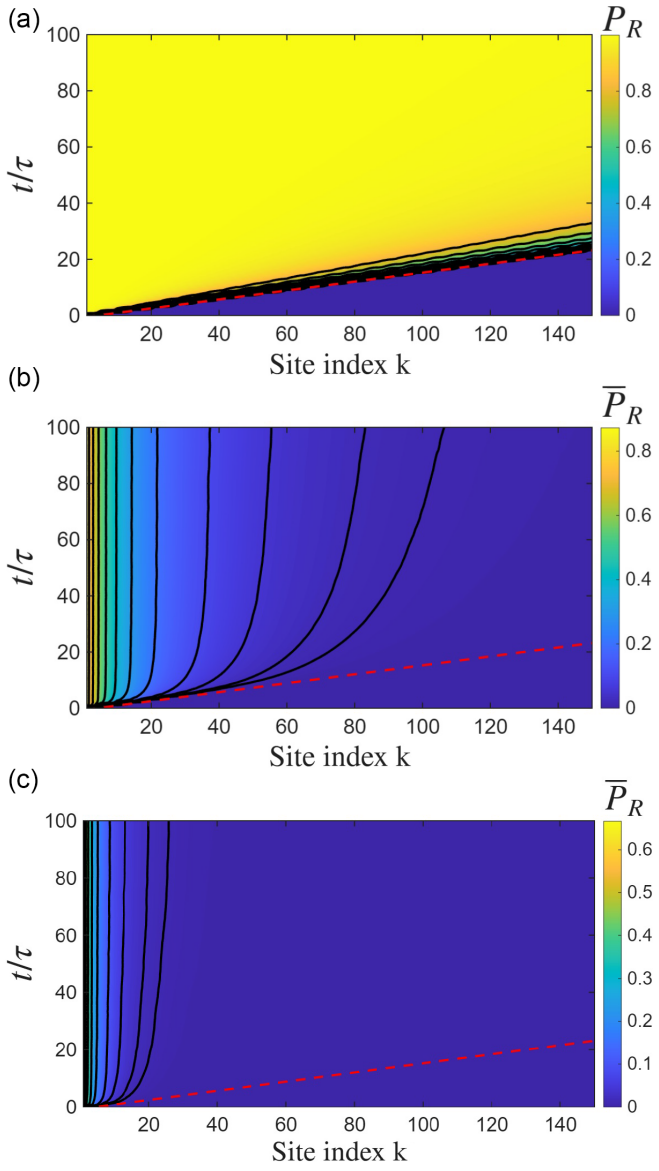

FIG. 18. Light-cone plots for 1D tight-binding chain of 300 sites. (a) The color indicates the probability of the particle being found to the right of site k, $P_R(k,t)$, for the case of no disorder, $\Delta\gamma = 0$. The color indicates the disorder-averaged probability $\overline{P}_R(k,t)$ for (b) weak disorder with $\Delta\gamma/\gamma = 1$ and (c) strong disorder with $\Delta\gamma/\gamma = 2$. The red dashed line in each plot corresponds to the velocity of Eq. (A4).

well-established single-particle Anderson localization in 1D. The light-cone curves (isocontours of $\overline{P}_R$) are bent upward by the presence of the disorder. Their shape is neither linear nor logarithmic. As time goes on, they in fact become vertical, indicating no further motion down the chain—zero propagation velocity.

This can be seen more explicitly by considering $\overline{P}_R$ at very long times. Figure 19 shows $\overline{P}_R$ for two long times, $t/\tau = 5000$ and 10 000, calculated for four different values of the probability distribution width. For each probability distribution, the result at the two times is identical, indicating that by these times there is no particle transport down the chain.

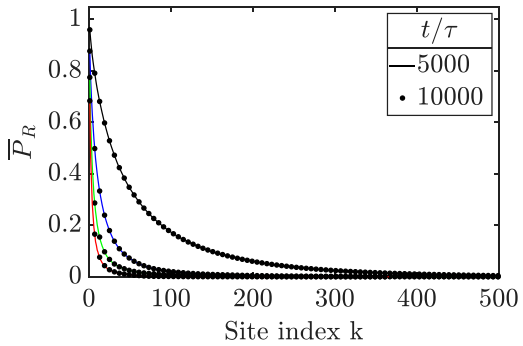

FIG. 19. Configuration-averaged probability $\overline{P}_R$ for two long times. The average is over 2000 sample configurations and $N = 600$. The disorder is characterized by $\Delta\gamma/\gamma_0 = 0.5$ (black), 1 (blue), 1.5 (green), and 2 (red).

4. Average versus typical values

We have defined the quantity $\overline{P}_R(k,t)$ in Eq. (A9) as the arithmetic mean over the set of sample disorder configurations. Variations in the hopping matrix element γ_k can be viewed as constituting a series of tunneling barriers and wells whose transmissions combine multiplicatively. This suggests using a geometric mean (log-average) to characterize the behavior of the set of random configurations. We define therefore the typical value of P_R by

$$P_R^{\text{typ}}(k,t) = \exp\left(\frac{1}{N_c}\sum_{m_c}^{N_c} \ln\left(P_R^{(m_c)}(k,t)\right)\right). \tag{A10}$$

Figure 20 compares $\overline{P}_R$ and P_R^{typ} for a disordered chain of $N = 1200$ sites with $\Delta\gamma/\gamma = 0.4$, $N_c = 10\,000$, and $t/\tau = 160$. By this time, multiple paths of interference have essentially extinguished propagation down the chain. On the left, where the average P_R is large, the two means differ only very slightly. For the light-cone diagrams of Fig. 18, the two measures would be indistinguishable from each other. But near the right, when the probability is very small, the distinction is worth noting. The inset of Fig. 20 shows the two means on

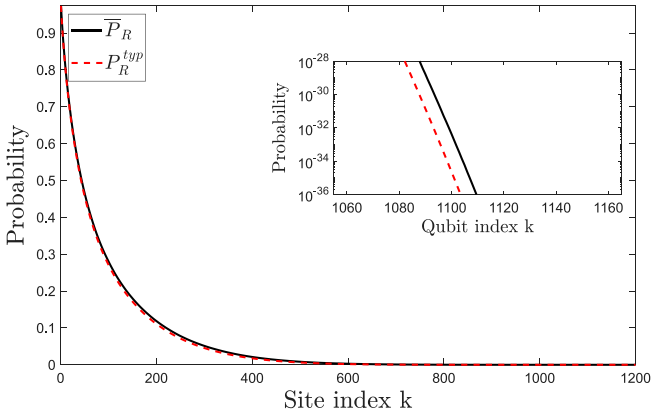

FIG. 20. The arithmetic mean and typical values of P_R over a set of $N_c = 10\,000$ samples. Here, the tight-binding chain has intersite coupling $\Delta\gamma/\gamma_0 = 0.4$ with $N = 1200$ sites and is evaluated at time $t/\tau = 160$. The inset shows the region around $k = 1100$ on a log scale.

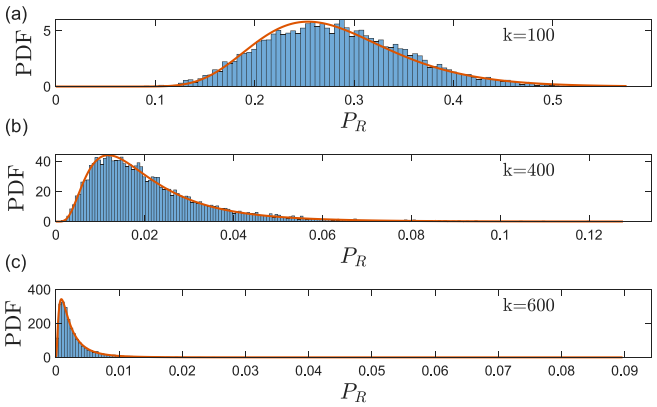

FIG. 21. The probability distribution function of the values of P_R for the same chain as in Fig. 20. Distributions are shown with a log-normal fit at three values of site index k.

a logarithmic scale in this region farther down the chain. The value of $\overline{P}_R$ in this region can be 2 orders of magnitude larger than P_R^{typ}.

The reason for this is made clear by considering the probability distribution function of P_R in the ensemble of samples. Figure 21 shows the probability distribution at three different points in the chain ($k = 100$, $k = 400$, and $k = 600$). The red line shows a fit to a log-normal distribution, which has a characteristically long tail. The figure's horizontal axis is chosen to include all the values of P_R, which occur in the 10 000 samples. One can see in Fig. 21(c) that some samples have a value of P_R that is more than an order of magnitude larger than the peak of the distribution. The arithmetic mean $\overline{P}_R$ is dominated by these relatively few "lucky" samples with a larger probability extending farther down the chain. The typical value defined by Eq. (A10) is then more useful.

APPENDIX B: FORMULATION WITH THE MAJORANA BASIS

1. Majorana definition and properties

There are $2N_q$ Majorana operators γ_j, one with an odd index and one with an even index for each qubit k. They are defined by

$$P_k \equiv \prod_{j<k} X_j, \quad P_1 = I,$$

$$\gamma_{2k-1} \equiv P_k Z_k, \quad \gamma_{2k} \equiv P_k Y_k. \tag{B1}$$

Each operates on the Hilbert space of the full chain, so each can be represented as a matrix of size $2^{N_q} \times 2^{N_q}$. Note that these γ_j are precisely the operators used in the Pauli walk described in Sec. II, as illustrated in Eq. (13).

The Majoranas satisfy

$$\gamma_k^2 = I, \quad \gamma_k = \gamma_k^\dagger, \tag{B2}$$

$$\{\gamma_i, \gamma_j\} = 2\delta_{i,j} I, \tag{B3}$$

$$[\gamma_m, \gamma_n] = 2\gamma_m \gamma_n, \quad m \neq n, \tag{B4}$$

$$[\gamma_j \gamma_k, \gamma_\ell] = 2\delta_{\ell,k}\gamma_j - 2\delta_{\ell,j}\gamma_k. \tag{B5}$$

Pauli operators can be expressed in terms of the Majorana basis,

$$X_k = i\,\gamma_{2k-1}\gamma_{2k}, \tag{B6}$$

$$Z_k = i^{k-1}\gamma_1\gamma_2\gamma_3\cdots\gamma_{2k-1} \tag{B7}$$

$$Z_k Z_{k+1} = i\gamma_{2k}\gamma_{2k+1}, \tag{B8}$$

$$Z_1 = \gamma_1, \quad Y_1 = \gamma_2. \tag{B9}$$

The full set of index-ordered Majorana strings, e.g., $G = \gamma_3\gamma_5\gamma_7$, forms an orthonormal basis for the whole operator space with the normalized Frobenius inner product,

$$\langle \mathcal{O}_1, \mathcal{O}_2 \rangle = \tfrac{1}{2^{N_q}} \text{Tr}(\mathcal{O}_1^\dagger \mathcal{O}_2), \tag{B10}$$

with the induced norm $\|\mathcal{O}\| = \sqrt{\langle \mathcal{O}, \mathcal{O} \rangle}$, as in Eq. (11). Two Majorana strings that differ in any index are orthogonal.

2. Majorana time development for a quadratic Hamiltonian

The Heisenberg equation of motion for γ_ℓ is

$$\frac{d\gamma_\ell(t)}{dt} = \frac{i}{\hbar}[H, \gamma_\ell(t)]. \tag{B11}$$

Consider a general Hamiltonian that is quadratic in Majorana operators:

$$H = \frac{i}{4}\sum_{m,n=1}^{2N_q} \mathcal{A}_{mn}\gamma_m\gamma_n, \tag{B12}$$

or equivalently

$$H = \frac{i}{4}\boldsymbol{\gamma}^T \mathcal{A}\boldsymbol{\gamma}, \quad \boldsymbol{\gamma} = \begin{pmatrix} \gamma_1 \\ \gamma_2 \\ \vdots \\ \gamma_{2N_q} \end{pmatrix}. \tag{B13}$$

The matrix $\mathcal{A}$ is real and antisymmetric, so H is Hermitian. The TFIM is a special case of this more general form. We will first find the Lieb-Robinson correlation function applicable to any quadratic Majorana Hamiltonian.

We can evaluate the commutator of a Majorana with the Hamiltonian using Eq. (B5),

$$[H, \gamma_\ell] = \frac{i}{4}\sum_{j,k=1}^{2N_q} \mathcal{A}_{jk}[\gamma_j\gamma_k, \gamma_\ell] \tag{B14}$$

$$= -i\sum_{j=1}^{2N_q} \mathcal{A}_{\ell j}\gamma_j. \tag{B15}$$

Therefore, Eq. (B11) becomes

$$\frac{d\gamma_\ell}{dt} = \frac{1}{\hbar}\sum_j \mathcal{A}_{\ell j}\gamma_j, \tag{B16}$$

or, using the vector of operators,

$$\frac{d\boldsymbol{\gamma}}{dt} = \frac{1}{\hbar}\mathcal{A}\boldsymbol{\gamma}. \tag{B17}$$

We can write the solution as

$$\boldsymbol{\gamma}(t) = e^{(\mathcal{A}/\hbar)t}\boldsymbol{\gamma}(0). \tag{B18}$$

It is useful to define this time evolution matrix $R(t)$ as

$$R(t) = e^{(\mathcal{A}/\hbar)t}, \tag{B19}$$

so

$$\boldsymbol{\gamma}(t) = R(t)\,\boldsymbol{\gamma}(0), \tag{B20}$$

or equivalently

$$\gamma_k(t) = \sum_m R_{km}(t)\,\gamma_m. \tag{B21}$$

R is a $2N_q \times 2N_q$ real orthogonal matrix.

3. Lieb-Robinson correlation function for a quadratic Hamiltonian

The Lieb-Robinson operator is

$$\hat{C}_k(t) \equiv [Z_1(t), Z_k]. \tag{B22}$$

To evaluate this, we can use Eq. (B7) and

$$Z_1(t) = \gamma_1(t) = \sum_m R_{1m}(t)\gamma_m \tag{B23}$$

to obtain

$$\hat{C}_k(t) = i^{k-1}\sum_{m=1}^{2N_q} R_{1m}(t)[\gamma_m, \gamma_1\gamma_2\gamma_3\cdots\gamma_{2k-1}]. \tag{B24}$$

For convenience, we define

$$M_k \equiv \gamma_1\gamma_2\gamma_3\cdots\gamma_{2k-1}. \tag{B25}$$

One can show that

$$[\gamma_m, M_k] = \begin{cases} 0, & \text{if } m \leqslant 2k-1, \\ 2\gamma_m M_k, & \text{if } m \geqslant 2k. \end{cases} \tag{B26}$$

Therefore, (B24) becomes

$$\hat{C}_k(t) = i^{k-1}\sum_{m=2k}^{2N_q} 2R_{1m}(t)\gamma_m M_k, \tag{B27}$$

where the sum over m now starts at $2k$.

The Lieb-Robinson correlation function is the normalized Frobenius norm of this operator. The Majorana strings $\gamma_m M_k$ are orthonormal, so we obtain simply

$$C_k(t) = 2\sqrt{\sum_{m=2k}^{2N_q} R_{1m}^2(t)} \tag{B28}$$

$$= 2\sqrt{\sum_{m=2k}^{2N_q} ([e^{(\mathcal{A}/\hbar)t}]_{1m})^2}. \tag{B29}$$

This is a general result for a quadratic Majorana Hamiltonian. It remains to find $\mathcal{A}$ for the TFIM and relate this to our result in Eq. (18).

4. The TFIM in Majorana basis

It can be shown from the fundamental relations in Appendix B 1 that the TFIM Hamiltonian [Eq. (5)] can be written as

$$H = -i\sum_{k=1}^{N_q-1} J_k\gamma_{2k}\gamma_{2k+1} - i\,\gamma\sum_{k=1}^{N_q}\gamma_{2k-1}\gamma_{2k}, \tag{B30}$$

where we use γ here (possibly confusingly) for the energy of the transverse field term as in Eq. (5). This can be written in the form of Eq. (B12) with

$$\mathcal{A} = -2\gamma\begin{pmatrix} 0 & 1 & 0 & 0 & 0 & 0 & \cdots & 0 \\ -1 & 0 & J_1' & 0 & 0 & 0 & \cdots & 0 \\ 0 & -J_1' & 0 & 1 & 0 & 0 & \cdots & 0 \\ 0 & 0 & -1 & 0 & J_2' & 0 & \cdots & 0 \\ 0 & 0 & 0 & -J_2' & 0 & \ddots & \vdots & \vdots \\ 0 & 0 & 0 & 0 & \ddots & \ddots & J_{N_q-1}' & 0 \\ \vdots & \vdots & \vdots & \vdots & \cdots & -J_{N_q-1}' & 0 & 1 \\ 0 & 0 & 0 & 0 & \cdots & 0 & -1 & 0 \end{pmatrix}. \tag{B31}$$

Comparing with Eq. (17), we see that

$$\mathcal{A} = -2\gamma A \tag{B32}$$

and

$$R(t) = e^{\mathcal{A}t/\hbar} = e^{-2\gamma At/\hbar}. \tag{B33}$$

Because $\tau = \pi\hbar/\gamma$, we can write this as

$$R(t) = e^{-2\pi(t/\tau)A}, \tag{B34}$$

and the expression for $C_k(t)$ in Eq. (B29) becomes

$$C_k(t) = 2\sqrt{\sum_{m=2k}^{2N_q}\left|\left[\exp\left(-2\pi\frac{t}{\tau}A\right)\right]_{1,m}\right|^2}, \tag{B35}$$

which is identical to the main operator Pauli walk result in Eq. (18).

[1] E. Lieb and D. Robinson, The finite group velocity of quantum spin systems, Commun. Math. Phys. **28**, 251 (1972).

[2] M. B. Hastings and T. Koma, Spectral gap and exponential decay of correlations, Commun. Math. Phys. **265**, 781 (2006).

[3] B. Nachtergaele, Y. Ogata, and R. Sims, Propagation of correlations in quantum lattice systems, J. Stat. Phys. **124**, 1 (2006).

[4] Z. Wang and K. R. A. Hazzard, Tightening the Lieb-Robinson bound in locally interacting systems, PRX Quantum **1**, 010303 (2020).

[5] A. Braida, S. Martiel, and I. Todinca, Tight Lieb–Robinson bound for approximation ratio in quantum annealing, npj Quantum Inf. **10**, 40 (2024).

[6] B. Hinrichs, M. Lemm, and O. Siebert, On Lieb-Robinson bounds for a class of continuum fermions, Ann. Henri Poincaré **26**, 41 (2025).

[7] R. Sweke, J. Eisert, and M. Kastner, Lieb–Robinson bounds for open quantum systems with long-ranged interactions, J. Phys. A: Math. Theor. **52**, 424003 (2019).

[8] L. Colmenarez and D. J. Luitz, Lieb-Robinson bounds and out-of-time order correlators in a long-range spin chain, Phys. Rev. Res. **2**, 043047 (2020).

[9] L. Cevolani, G. Carleo, and L. Sanchez-Palencia, Spreading of correlations in exactly solvable quantum models with long-range interactions in arbitrary dimensions, New J. Phys. **18**, 093002 (2016).

[10] M. C. Tran, C.-F. Chen, A. Ehrenberg, A. Y. Guo, A. Deshpande, Y. Hong, Z.-X. Gong, A. V. Gorshkov, and A. Lucas, Hierarchy of linear light cones with long-range interactions, Phys. Rev. X **10**, 031009 (2020).

[11] J. T. Schneider, J. Despres, S. J. Thomson, L. Tagliacozzo, and L. Sanchez-Palencia, Spreading of correlations and entanglement in the long-range transverse Ising chain, Phys. Rev. Res. **3**, L012022 (2021).

[12] J.-B. Bru and W. de Siqueira Pedra, *Lieb-Robinson Bounds for Multi-commutators and Applications to Response Theory* (Springer, Cham, Switzerland, 2016), Vol. 13.

[13] C.-F. A. Chen, A. Lucas, and C. Yin, Speed limits and locality in many-body quantum dynamics, Rep. Prog. Phys. **86**, 116001 (2023).

[14] C.-F. Chen and A. Lucas, Optimal Frobenius light cone in spin chains with power-law interactions, Phys. Rev. A **104**, 062420 (2021).

[15] P. W. Anderson, Absence of diffusion in certain random lattices, Phys. Rev. **109**, 1492 (1958).

[16] J. Fröhlich and T. Spencer, Absence of diffusion in the Anderson tight binding model for large disorder or low energy, Commun. Math. Phys. **88**, 151 (1983).

[17] B. M. McCoy and T. T. Wu, Theory of a two-dimensional Ising model with random impurities. I. Thermodynamics, Phys. Rev. **176**, 631 (1968).

[18] P. Pfeuty, An exact result for the 1D random Ising model in a transverse field, Phys. Lett. A **72**, 245 (1979).

[19] R. B. Griffiths, Nonanalytic behavior above the critical point in a random Ising ferromagnet, Phys. Rev. Lett. **23**, 17 (1969).

[20] F. Igloi and C. Monthus, Strong disorder RG approach of random systems, Phys. Rep. **412**, 277 (2005).

[21] J. Kisker and A. P. Young, Dynamical critical properties of the random transverse-field Ising spin chain, Phys. Rev. B **58**, 14397 (1998).

[22] J. A. Hoyos and T. Vojta, Dissipation effects in random transverse-field Ising chains, Phys. Rev. B **85**, 174403 (2012).

[23] C. K. Burrell and T. J. Osborne, Bounds on the speed of information propagation in disordered quantum spin chains, Phys. Rev. Lett. **99**, 167201 (2007).

[24] M. Friesdorf, Closed quantum systems and localization, Ph.D. thesis, University of Cologne, Cologne, Germany, 2015.

[25] Y. Zeng, A. Hamma, Y.-R. Zhang, Q. Liu, R. Li, H. Fan, and W.-M. Liu, Logarithmic light cone, slow entanglement growth, and quantum memory, Phys. Rev. B **112**, 094202 (2025).

[26] C. L. Baldwin, A. Ehrenberg, A. Y. Guo, and A. V. Gorshkov, Disordered Lieb-Robinson bounds in one dimension, PRX Quantum **4**, 020349 (2023).

[27] C. L. Baldwin, Subballistic operator growth in spin chains with heavy-tailed random fields, Phys. Rev. B **111**, 184204 (2025).

[28] M. Gebert and M. Lemm, On polynomial Lieb–Robinson bounds for the XY chain in a decaying random field, J. Stat. Phys. **164**, 667 (2016).

[29] D. Damanik, M. Lemm, M. Lukic, and W. Yessen, On anomalous Lieb–Robinson bounds for the Fibonacci XY chain, J. Spectr. Theory **6**, 601 (2016).

[30] E. Hamza, R. Sims, and G. Stolz, Dynamical localization in disordered quantum spin systems, Commun. Math. Phys. **315**, 215 (2012).

[31] H. Abdul-Rahman, B. Nachtergaele, R. Sims, and G. Stolz, Localization properties of the disordered XY spin chain, Ann. Phys. (N.Y.) **529**, 1600280 (2017).

[32] B. J. Mahoney and C. S. Lent, Lieb-Robinson correlation function for the quantum transverse-field Ising model, Phys. Rev. Res. **6**, 023286 (2024).

[33] M. Acharyya, Y. Holovatch, and F. Iglói, 100 glorious years of the Ising model, Eur. Phys. J. B **99**, 16 (2026).

[34] P. Steinacker, T. Tanttu, W. H. Lim, N. D. Stuyck, M. Feng, S. Serrano, E. Vahapoglu, R. Y. Su, J. Y. Huang, C. Jones, *et al.*, Bell inequality violation in gate-defined quantum dots, Nat. Commun. **16**, 3606 (2025).

[35] N. C. Chiu, E. C. Trapp, J. Guo, M. H. Abobeih, L. M. Stewart, S. Hollerith, P. L. Stroganov, M. Kalinowski, A. A. Geim, S. J. Evered, *et al.*, Continuous operation of a coherent 3,000-qubit system, Nature (London) **646**, 1075 (2025).

[36] A. D. King, A. Nocera, M. M. Rams, J. Dziarmaga, R. Wiersema, W. Bernoudy, J. Raymond, N. Kaushal, N. Heinsdorf, R. Harris, *et al.*, Beyond-classical computation in quantum simulation, Science **388**, 199 (2025).

[37] E. Lieb, T. Schultz, and D. Mattis, Two soluble models of an antiferromagnetic chain, Ann. Phys. (N.Y.) **16**, 407 (1961).

[38] S. Sachdev, *Quantum Phase Transitions* (Cambridge University Press, Cambridge, UK, 2011), 2nd ed.

[39] F. Igloi and G. Tóth, Entanglement witnesses in the *XY* chain: Thermal equilibrium and postquench nonequilibrium states, Phys. Rev. Res. **5**, 013158 (2023).

[40] B. J. Mahoney and C. S. Lent, The value of the early-time Lieb-Robinson correlation function for qubit arrays, Symmetry **14**, 2253 (2022).

[41] D. S. Fisher, Critical behavior of random transverse-field Ising spin chains, Phys. Rev. B **51**, 6411 (1995).

[42] H. Rieger and A. P. Young, Griffiths singularities in the disordered phase of a quantum Ising spin glass, Phys. Rev. B **54**, 3328 (1996).

[43] I. A. Kovács and F. Iglói, Geometry of rare regions behind Griffiths singularities in random quantum magnets, Sci. Rep. **12**, 1074 (2022).

[44] P. Calabrese and J. Cardy, Time dependence of correlation functions following a quantum quench, Phys. Rev. Lett. **96**, 136801 (2006).

[45] P. Calabrese and J. Cardy, Quantum quenches in extended systems, J. Stat. Mech. (2007) P06008.

[46] H. Rieger and F. Iglói, Semiclassical theory for quantum quenches in finite transverse Ising chains, Phys. Rev. B **84**, 165117 (2011).

[47] W. P. Su, J. R. Schrieffer, and A. J. Heeger, Solitons in polyacetylene, Phys. Rev. Lett. **42**, 1698 (1979).

[48] N. Batra and G. Sheet, Physics with coffee and doughnuts, Resonance **25**, 765 (2020).

[49] G. Roósz, Y.-C. Lin, and F. Iglói, Critical quench dynamics of random quantum spin chains: Ultra-slow relaxation from initial order and delayed ordering from initial disorder, New J. Phys. **19**, 023055 (2017).